ACS APPLIED NANO MATERIALS

Article

Nanosize and Shape Effects on Antimicrobial Activity of Silver Using Morphology-Controlled Nanopatterns by Block Copolymer Fabrication

Tandra Ghoshal, Malco Cruz-Romero, Joseph P. Kerry, and Michael A. Morris

ACS Appl. Nano Mater., **Just Accepted Manuscript** • DOI: 10.1021/acsanm.9b01286 • Publication Date (Web): 04 Oct 2019

Nanosize and Shape Effects on Antimicrobial Activity of Silver Using Morphology-Controlled Nanopatterns by Block Copolymer Fabrication

Tandra Ghoshal,†* Malco C. Cruz-Romero,± Joseph P. Kerry,± Michael A. Morris†*

†School of Chemistry, AMBER and CRANN, Trinity College Dublin, Dublin, Ireland, D02AK60

±Food Packaging group, School of Food and Nutritional Sciences, University College Cork, Cork, Ireland, T12 YT20

[*] Corresponding Author:

Prof. Michael A. Morris

Tel: +353 1 896 3089

Fax: +353 1 896 3089

E-mail: morrism2@tcd.ie

And

Dr. Tandra Ghoshal

Email: g_tandra@yahoo.co.in

ABSTRACT: The activity of silver nanomaterials as an antimicrobial is well known with authors noting strong size and shape effects. This paper explores if the antimicrobial activity relates to unique size related properties of the nanodimensioned materials or a more physical effect. *Staphylococcus aureus* and *Pseudomonas aeruginosa* were explored as test bacteria. They can cause serious human infections and are becoming resistant to pharmaceutical antimicrobials. Silver nanopatterns on a substrate surface were used as the antimicrobial agent. We demonstrate a cost-effective facile route to fabricate well-ordered, periodic and dimension-controlled silver lines and dots pattern on a substrate surface. This allowed precise definition of the silver materials to explore size and shape effects. Polystyrene-*b*-poly(ethylene oxide) (PS-*b*-PEO) block copolymer (BCP) microphase separated thin films were used as structural templates. Well-ordered PS-*b*-PEO thin film with vertical and parallel oriented PEO cylinders were achieved by a solvent vapour annealing approach through careful optimization of experimental parameters. A selective inclusion method (into one block of the BCP) of silver nitrate was used to generate the silver nanopatterns. Spin coating precursor-ethanol solution and subsequent UV/ozone treatment produces silver nanopattern arrays. They exhibited a significant growth-inhibitory effect on *Staphylococcus aureus* and *Pseudomonas aeruginosa* biofilms. However, data suggests this is associated with high surface area rather than a unique nanodimension related property change dictated by size or shape.

Keywords: Silver, nanopatterns, block copolymer, self-assembly, substrate, optical, antimicrobial, surface area.

1. INTRODUCTION

The synthesis of silver nanostructures and patterns has been an attractive area because of the broad range of applications of silver materials in catalysts, scanning probe spectroscopies, electronics and nanophotonics.[1-3] The strong optical absorption and fluorescence of silver nanoparticles and silver nanowires make them of special interest because silver demonstrates optical response in the visible range. The fabrication of nanodimensioned, size-controlled and periodic arrays (nanopatterning) is essential for the optimum performance of many devices. Nanopatterning is generally performed by various techniques, principally by lithography[4] and these methods yield high-quality patterns but involve complicated multistep processing, expensive facilities and are generally high energy and potentially polluting.[5,6] As an alternative, self-assembly can be used where periodic and even aligned (directed self-assembly (DSA)) nanostructures are generated by enthalpic self-assembly (i.e. microphase separation) and secondary interactions that define the alignment direction.[7] The microphase separation of block copolymers (BCPs) appears to be a promising technique to form highly regular periodic nanodimensioned arrangements resulting from the minimisation of the surface area between incompatible blocks.[8-11] In thin films, the interfacial energies of the solid substrate and the air interface can contribute appreciably to the morphological arrangement of BCP thin films. The solvent annealing approach has proved to be efficient in generating ordered BCP arrangements through swelling of the polymers by solvent/s creating free volume to allow chain movement and reptation.[12,13] Many strategies have been reported to manipulate interfacial (polymer/substrate or polymer/air) interactions to control feature orientation of the microdomains.[14-18]

As previously reported by us[19-23] we have demonstrated the fabrication of oxide nanodot and line patterns based on solvent-mediated microphase separation in PS-*b*-PEO thin films. These films have precise structure and orientation. An advantage of these materials is the

noticeable difference in the chemical selectivity of PS and PEO to solvents. Generally, methods such as UV degradation, ozonolysis reactive ion etching and chemical etching can be used to selectively remove the minority block in BCPs. But the poor degradability of PEO hinders the process to generate nanopores from PS-*b*-PEO thin films without noticeable pattern damage.[24-25] Generally dry etching of one of the blocks followed by the precursor deposition or selective functionalization of polymer/metal precursor has been used to incorporate metal species within the pores.[26-27] However, these methods are limited in terms of expensive complicated fabrication equipment and the material sets that can be used. Comparatively, the methodology reported here is based on a simple, general solvation method rather than complicated co-ordination chemistry between metal precursors and one of the polymer blocks and further, it is not an essential step to remove the block by dry etch to create nanoporous template. The cylindrical phase of the BCP is used here since the domain orientation is relatively easily controlled through a solvent annealing approach. It is also useful for our infiltration method that both domains are present at the air-surface interface allowing ease of penetration.

A common issue is that the patterned nanostructures are weakly bonded with the substrate. In order to strengthen the bonding between the networks and the substrate, methods of using surface functionalization, mixing with other functional materials, light exposure, mechanical pressure, and encapsulating with a capping layer have been reported.[28-31] Here we show patterns can be simultaneously fabricated and be strongly adhered to the surface using UV/ozone treatments after inclusion of desired materials.

Microbial surface contamination has become extensive and of significant concern worldwide. Microorganisms adhere and grow rapidly on surfaces such as medical devices, wound dressing, food packages, separation membranes under appropriate atmospheric conditions.[32-33] Moreover, it is difficult to remove them completely because of the persistent nature of the microorganisms. As a broad-spectrum antimicrobial material, nanosilver exhibits

excellent antimicrobial properties specify physiochemical characteristics. A critical question is the antimicrobial activity of silver is due to unique property changes of the particles because of small size or just a surface area effect.[34] Herein, bioactive surface coating with silver nanostructure arrays with precisely controlled sizes and shapes were fabricated to gain insight to the nano-mechanism of antimicrobial activity that destroy adherent and surrounding microorganisms through controlled release of silver ions.[35] Results strongly support a surface area related effect with little indication of unique property changes due to nanodimesnion.

2. EXPERIMENTAL SECTION

2.1. Materials.

Two different polystyrene-b-poly(ethylene oxide) (PS-*b*-PEO) di-BCPs were purchased from Polymer Source Inc. and used without further purification (number-average molecular weight, M_n, PS = 32 kg mol^{-1}, M_n, PEO = 11 kg mol^{-1}, M_w/M_n = 1.07, M_w: weight-average molecular weight and PS = 62 kg mol^{-1}, M_n, PEO = 16 kg mol^{-1}, M_w/M_n = 1.08). Both BCPs form hexagonal arrangements of PEO cylinders in a PS matrix. Single crystal B doped P type silicon (Si) wafers with (100) crystalline orientation and with the usual thin passive oxide film were used as a substrate (2 x 2 cm^2). Toluene (99.9%), Tetrahydrofuran (THF, 99.9%), anhydrous alcohol (≥99.9%) and silver nitrate ($AgNO_3$, ≥99.0%) were purchased from Sigma-Aldrich and used without further purification.

2.2. Preparation of silver nanostructure arrays by block copolymers.

Substrates were cleaned in acetone and toluene for 30 minutes by ultrasonication respectively and dried under nitrogen stream. PS-*b*-PEOs was dissolved in toluene to achieve 1 wt% solution (0.01 gm polymer in 9.99 gm toluene) and stirred for at least 12 h at room temperature. The PS-*b*-PEO thin films were spin coated from a polymer solution (3000 rpm for 30 s). Self-assembly was achieved by exposure to various solvent atmospheres (3 ml toluene, 3 ml THF and 1.5 ml/1.5 ml toluene/THF) for controlled periods of time and

temperature to induce the required chain swelling and interactions to promote microphase separation. The solvents, temperature (50 and 60° C) and time (30 mintutes to 3h) were varied to achieve optimum phase separated, periodic patterns. Partial etching/modification of PEO domains was realized by ultrasonication at room temperature in anhydrous alcohol (20 ml) for different times (varied from 15-25 minutes to achieve optimum time) as dictated by the BCP molecular weight. The film was removed from the solvent after the desired ultrasonication time and dried immediately. For the fabrication of silver nanopatterns, $AgNO_3$ was dissolved in anhydrous ethanol (0.4 wt %, 0.04 gm $AgNO_3$ in 9.96 gm anhydrous alcohol) by ultrasonication for 30 minutes and spin-coated onto the activated film template. The concentrations of silver nitrate were calibrated to fabricate desired nanostructures and to avoid any overfilling or discontinuity of the patterns. UV/Ozone treatment at room temperature for 3 h was used to form silver nanopatterns and remove polymer[23]. The UV light (185 nm) generates ozone from atmospheric oxygen. The ozone is the active oxidizing agent, creating atomic oxygen which reacts with the polymer to form carbon dioxide, water and volatile organic compounds. The process steps for the formation of silver nanodots and line patterns are described by Scheme 1.

2.3. Characterizations.

The Cole-Parmer ultrasonic cleaner 8891 was used for ultrasonication treatment. The solvent annealed patterned films were inserted in anhydrous alcohol at room temperature placed at a flat bottom glass container. Surface morphologies were revealed by scanning probe microscopy (SPM, Park systems, XE-100) in tapping mode as well as scanning electron microscopy (SEM, FEI Company, FEG Quanta 6700 and Zeiss Ultra Plus). Film thicknesses were measured by ellipsometery (Woolam M2000) together with SEM. Cross sectional TEM (transmission electron microscopy) samples were prepared using an FEI Helios Nanolab 600i system containing a high resolution Elstar™ Schottky field-emission SEM and a Sidewinder

FIB column and were imaged by TEM (JEOL 2100 and TEM, FEI Titan). X-ray diffraction (XRD) graphs were recorded on a PANalytical MPD instrument equipped with an Xcelerator detector and Cu Kα anode (45 kV and 40 mA). The absorption spectra were measured with a spectrophotometer (Cary 50) in a reflectance mode. The substrates were placed directly within the instrument with the substrate holder adapter. Room temperature photoluminescence measurements were made with a luminescence spectrometer (Perkin Elmer LS 50 B, 325 nm excitation wavelength).

2.4. In vitro Antimicrobial Activity.

The antimicrobial activity of the Ag nanopatterns was evaluated against *Staphylococcus aureus* (gram positive bacteria) and *Pseudomonas aeruginosa* (gram negative bacteria). For comparison and to achieve a greater antimicrobial activity, multiple coatings of silver on glass substrates were examined. This is studied for two different silver nanopatterns for a monolayer, 2 and 4 times coated films. For the multiple layer coating, same precursor solution was spin coated and UV/Ozone treated repeatedly for each coating. After each coating, the substrate was washed with water to remove any excess unattached silver. Bacteria were grown in Muller-Hinton broth (MHB) for 18 h at 30 or 37 °C under constant agitation on an orbital shaker at 170 rpm. The final bacterial load was 10^9 colony forming units per milliliter of culture ($CFUml^{-1}$). For this purpose, silver nanopatterns were fabricated on glass substrates. Glass substrates without silver nanopatterns were used as a control. All samples were incubated for 24 hours at the same temperatures during the inoculation procedure. The concentrations of the silver nanopatterns were varied to achieve optimum antimicrobial activity.

2.5. Statistical analysis.

All data was analysed using standard deviations and analysis of variance. One-way analysis of data variance was calculated using SPSS 21 for Windows (SPSS Statistical Software, IBM

Corp., NY, USA) software package. A difference between pairs of means was resolved by means of confidence intervals using Tuckey's test. The level of significance was set at $p<0.05$.

3. RESULTS AND DISCUSSION

3.1. Control of block copolymer nanopatterns.

Size and morphological variation of the nanopatterns was accomplished by using different molecular weight BCPs. Polymers are represented as S1 (32k-11k) and S2 (62k-16k) as described below. The two different molecular weight BCPs were selected to generate two different kind of nanofeatures with different dimension described as nanolines and nanodots depending on their molecular weight and volume fraction of the constituent blocks. The as-coated films exhibited little or no indication of periodic ordering. Solvent annealing was used to selectively achieve vertical and horizontal orientation of PEO cylindrical microdomains in the PS matrix and, thus, produce two different shapes of nanomaterials, dots and lines. To achieve optimum ordering and size control, the annealing solvent/s, temperature and time were varied. Films were solvent annealed at 50 and 60° C in toluene, tetrahydrofuran (THF) or toluene/THF mixed solvents for different times to define the structure and orientation of the cylindrical arrangement formed for each BCP. Figure 1 gives representative AFM data for BCP S1 after the toluene exposure at 50 ℃ for different times of 15 min to 3 h (line patterns). Note, THF and mixed solvent annealing gave ordered arrangements, but dewetting of the as cast continuous film occurred to form islands at a greater thickness. For toluene, mostly micellar structures were formed after spin coating and after 15 min (Figure 1a) of toluene exposure. One observes poor microphase separated features with a mixed perpendicular and parallel orientated PEO cylinders for 30 min (Figure 1b) exposure; however well-ordered "fingerprint" patterns with parallel PEO cylinders are seen for longer time periods of 45 minutes (see supporting information, Figure S1), 1h (Figure 1c) and 1 h 30 min (Figure 1d). For longer time periods of 2 h (Figure 1e) and 3 h (Figure 1f), long range ordered line-type patterns with parallel PEO

cylinder orientation were achieved as shown in Schematic (IIA). The films are of regular thicknesses of 25 nm as measured by ellipsometry and no sign of dewetting was observed. Higher annealing temperature and time leads to poor coverage and patterns. The average distance between adjacent microdomains is 32 nm and the PEO cylinder diameter is 17 nm. No noticeable differences in the arrangement on glass, quartz, silica etc. were observed.

The higher molecular weight BCP S2 was used to increase feature size and spacing and alter cylinder orientation (dot patterns). Both toluene and THF solvent annealing gives either partial phase separation and/or poor ordering of the microdomains at a temperature of 50 ℃ and 60 ℃ for times between 15 min to 2 h (see supporting information, Figure S2). In comparison, a 50:50 volume ratio of toluene/THF solvents provided ordered domains arrangements. Figure 2 shows the AFM images of S2 after microphase separation annealed (60 ℃) for different times. 30 min annealing gave periodic arrangements with perpendicular orientation of the PEO cylinders (Figure 2a) though thickness and coverage were not homogeneous. Increasing the solvent exposure time to 1 h gave periodic dot patterns with PEO cylinder diameter of 38 nm with a lateral spacing of 72 nm as shown in Figure 2b and Schematic (IA). These films exhibited regular thicknesses of 75 nm as measured by ellipsometry and no dewetting occurred. Similar patterns were observed for longer times of 1 h 30 min (Figure 2c), but thickness variation throughout the film noticed suggesting the start of dewetting. Longer exposure time of 2 h 30 min leads to thickness variation and patterns missing in most of the places described in the supporting information, Figure S3.

Previous work suggests that the phase separated films have a PEO layer at the polymer-substrate interface due to favourable PEO-substrate interactions. In contrast, a PS layer is formed by segregation to the polymer-air interface since PS has a lower surface energy, γ_{PS} = 33 mNm^{-1}; γ_{PEO} = 43 mNm^{-1}.[19] The optimum solvent/s for solvent annealing were dependent on the molecular weight and volume fraction of PS (f_{PS}) and PEO (f_{PEO}) of the blocks. The f_{PS}

and f_{PEO} values for S1 and S2 are 0.748, 0.798 and 0.252, 0.202 respectively. Parallel cylinder orientation was achieved by toluene vapour annealing for f_{PS} values < 0.75 whereas perpendicular orientation preferred for toluene/THF mixed solvent vapours for $f_{PS} > 0.75$. PEO has larger solubility parameter difference though it dissolves in toluene and THF, ($\delta_{Tol} - \delta_{PEO}$ =1.9 $MPa^{1/2}$, $\delta_{THF} - \delta_{PEO}$ = 3.4 $MPa^{1/2}$) than PS ($\delta_{Tol} - \delta_{PS}$ = 0.3 $MPa^{1/2}$, $\delta_{THF} - \delta_{PS}$ = 1.2 $MPa^{1/2}$). Thus, both toluene and THF enhances swelling and impart increased chain mobility of the PS chains compared to PEO. The vapour pressure of toluene and THF are 3.09 kPa and 17.7 kPa (at 21° C) respectively also contribute to the rate of the swelling process and solvent density can affect the self-assembly morphology [13]. For sample S1, a toluene vapour environment provided necessary chain mobility and swelling because of lower molecular weight. For S2 with larger molecular weight and a greater PS volume fraction extra driving force to rearrange the blocks was needed and THF was used which has higher vapour pressure and is selective to PS. However, it is associated with pattern degradation and thickness variation possibly due to high swelling. Toluene/THF mix vapours were used to achieve optimum chain mobility and swelling of the PS and PEO chains so that long range ordered structures can be obtained.

From Figures 1 and 2, it is noted that the lower molecular weight BCP S1 favours parallel orientation whereas S2 generates vertical orientation of the cylinders. Since PEO cylinders are limited to the thickness of the films, shorter solvent annealing periods results in vertical orientation for S1 as this is kinetically least hindered. At extended periods the cylinders can re-orientate into a parallel orientation as the kinetics become less limited and the PS matrix is formed at the surface. The parallel orientation is thermodynamically favourable at a thickness equal to the cylinder-cylinder spacing ~32 nm. Thus, the thinner film (S1) exhibits the greatest tendency to produce a stable parallel arrangement and the thicker film (S2) show increased probability of forming vertical orientations.[21-22] For S2, the increased thickness of the film ensures that a higher temperature is required to swell the film through its entire thickness range.

Note that the thickness of the films has an effect on defect density. At greater thickness, the evaporation process following solvent annealing is slower resulting in glassification and solvent trapping. Surface defects can be initiated due to trapped solvent modifies the polymer-substrate, polymer-air and polymer-polymer interactions.[21-22] Thus, the increased periodicity of the thinner films is likely due to the presence of less residual solvent.

3.2. Fabrication of nanoporous template.

To enable process reproducibility for metal ion infusion it was necessary to modify the PEO block. This was achieved by an ultrasonic ethanol method which degrades the PEO domains improving uptake of ions. No noticeable change in the structural arrangement and dimensions is realized after ethanol treatment as can be seen in Figure 3. The optimized sonication times are 18 and 22 min for S1 and S2 respectively. Variation of the sonication time resulted in partial etch, surface roughness or pattern degradation. Figures 3a, b and g shows SEM images of the nanoporous line and dot templates after ethanol exposure of S1 and S2 respectively. The AFM phase contrast increases whilst maintaining the long-range order is seen in the images. Additionally, the cylinder-cylinder spacings, the PEO cylinder diameters and the film thicknesses (measured by ellipsometer) remained same from as-synthesised films. Also, the high long range order of the nanoporous template was preserved.[36] This is described as Schematic (IB and IIB).

3.3. Structural arrangement of the nanoporous templates by FIB and TEM.

The effect of the ethanol ultrasonication step was assessed by cross-sectional TEM. The effect of ethanol treatment was investigated for two different periods of ultrasonication times of 14 (Figures 3c and d) and 18 minutes (Figures 3e and f) for S1. The polymer templates were well attached to the substrate surface without any indication of deformation or delamination. In the films, the ‘nanopores’ extend to a specific depth through the film thickness. It is clear from the images that the treatment predominantly affects the PEO component. A partial PEO

etch starting from the top surface of the film was realized for smaller ultrasonication time and formed elliptically shaped pores. These pores do not reach the substrate surface as 4 nm dense PS layer exists at this interface as suggested in earlier work.[20] Increased exposure time showed that the nanopores extend through the entire thickness of the film. It was not possible to measure the actual thicknesses of the films after the ethanol exposure because platinum was deposited during FIB lamellae preparation which diffuses into the surface of the polymer film. The diameters of the nanopores are18 nm for S1 as measured from the higher magnification images in Figure 3d and 3f. If the pore depth shown in Figures 3d and 3f are compared, it is obvious that the ethanol treatment is ono-linear with time. It is proposed that PEO removal involves two steps; swelling of the PEO followed by solution with the swelling being kinetically limiting. Similar statistics were obtained for S2 after the optimized 22 min ultrasonication (inset of Figure 3g). For S2, the effect of platinum deposition is somewhat less might be because of bigger pore sizes. The diameters and depths of the PEO cylinders were 38 and 48 nm respectively with a 24 nm thick PS wetting layer at the substrate. The PS is amorphous in nature.

3.4. Mechanism for the formation of nanoporous templates.

A probable mechanism to create the nanoporous templates was proposed previously.[19-22] It was suggested that the acoustic cavitation created by ultrasonication in the presence of solvent generates free radicals which assists the bond cleavage of the PS-*b*-PEO. Ethanol was the preferred etchant because of its vapour pressure and ability to swell and eventually dissolve the block. The cavitation within the inactive polymer is a result of the solvent in the swollen polymer film. Acoustic cavitation is more powerful for lower vapour pressure solvents (5.95 kPa at 20^0 C for ethanol).[37] It is postulated that swelling is significant and under this treatment the PEO chains become isolated in the solvent and this allows them to be fully solvated.[38] The PEO molecules cannot be isolated themselves from the solution upon termination of

ultrasound, because those PEO monomers are undistinguishable from ethanol molecule. This resulted to form a crystalline layer of the PEO chains whereas some of the ethanol molecules trapped in the adjacent regions.[38]

3.5. Generation of silver nanoarrays: Morphological, spatial and dimensional control.

The silver metal nanostructure arrays were generated by selective inclusion of metal ions (via spin-coating of ethanolic solution) (Scheme (I and II C)) coupled to a subsequent UV-Ozone treatment (Scheme (I and II D)). Figure 4 shows the SEM images of periodic silver nanoline and naodot arrays (S1 and S2 respectively) with a difference in their diameters and spacings (compared to unfilled systems). All the infiltrated nanostructures are uniform and the size/shape are similar to the parent BCP patterns. The average diameters of the nanolines and nanodots were 14 ± 2 nm (Figures 4a-b), 35 ± 4 nm (Figure 4c) for S1 and S2 respectively. The precursor concentrations were carefully optimized to fabricate uniform and continuous patterns. Changes of the solution concentration results in either discontinuous, poor patterns or overlapping of the nanostructures. The increment in solution concentrations used in S1 and S2 is probably related to the increased pore volume for the higher molecular weight BCP films. The average nanoline heights were 4-6 nm whereas nanodot heights were between 6-10 nm (by ellipsometry). The density of the features on the substrate is measured approximately 3.12 x 10^5 lines cm^{-1} and 3.85 x 10^{10} nanodots cm^{-2}.

3.6. Silver nanoarrays: Crystallinity and phases.

The crystallinity and phase purity of the metallic nanostructures were investigated by XRD, EDAX and TEM analysis. For the TEM analysis, Si substrate containing nanodots were scratched and dispersed in anhydrous ethanol by ultrasonication and dropped onto a TEM grid. A TEM image of a set of removed nanodots are shown in Figure 4d. They can be seen to be hemi-spherical in shape and crystalline in nature. The diameters of the nanodots ranged from 30-40 nm. The inset of Figure 4d shows a crystalline hemispherical nanodot of diameter of 35

nm. This is polycrystalline in nature and grain boundary defects are visible. As similar strategy was followed to generate the silver nanolines, comparable crystallinity is expected for the nanoline feature.

XRD analysis of both nanopatterns shows similar results and a representative diffractogram is shown in Figure 4e. The two diffraction peaks observed indicate the face-centered cubic silver (JCPDS file No. 04-0783) structure. The 2θ values of the peaks (38.24° and 44.42°) are (111) and (200) reflection planes respectively.[39-40] This illustrates phase pure silver metal, no peaks from oxides and other impurities were detected.

EDX spectra also confirms the presence of silver. Figure 4f shows the predominant peaks of silver. The O and Si peaks were readily comes from the Si substrate.

3.7. Silver nanoarrays: Optical properties.

The optical properties are consistent with the nanodimension of the materials. The UV-vis spectra of the patterns were investigated. Both line and dot nanostructures show the characteristic (the transverse plasmon excitation of silver nanostructures[41-42]) absorption peak at around 410 nm (Figure 5a). The intensity for the silver nanolines is higher than the nanodots consistent with the higher surface coverage (see below) seen for this arrangement. A representative spectrum is shown in Figure 5a. Room temperature photoluminescence (PL) emission properties are observed under excitation wavelength of 350 nm for both the nanoline and nanodot patterns. Blue-green PL emission observed at around 470 nm (Figure 5b) can be attributed to Ag^{+} and Ag^{+}- Ag^{+}[43]. The PL peak is readily assigned to radiative recombination of Fermi level electrons and sp- or d-band holes as seen for other noble metals.[41,44]

3.8. Antimicrobial study.

The antibacterial activity of silver nanopatterns were examined in vitro with two different kind of bacteria, *Staphylococcus aureus* (gram-positive bacteria) (Figure 6a, b) and *Pseudomonas aeruginosa* (gram-negative bacteria) (Figure 6c, d). The antimicrobial effects of

both patterns are obvious as shown in Figure 6 and Table 1. Data reported here are from samples with four coatings (on glass) of silver to increase the silver concentrations. The inhibition zones using a diffusion-type assay method against a glass substrate control sample (not shown) and silver nanopatterns clearly indicates better antimicrobial effect for the nanoline patterns compared to nanodots. It is tempting to explain the additional activity of the lines due to smaller feature size (line diameter is 14 nm whilst the dot diameter is 35 nm) and a nano defined property change of the silver. However, the surface area of the nanolines and nanodots vary also and should be considered. Using a cylinder shape for the nanodots and a hemispherical line profile (consistent with TEM profiles described above) as well as dimensions measured therefrom, the surface area of the features can be calculated as 0.68 (lines) and 0.54 cm^2 for 1 cm^2 of substrate. The ratio of the surface area of silver for S1 to S2 (~1.26) is consistent with the ratio of values of the corresponding measured inhibition zone areas shown in Table 1. As the inhibition zone area corresponds to the quantity the antimicrobial activity, it can be concluded that Figure 6e indicates the ratio of the efficiency of antimicrobial activity for S1 to S2 as a function of number of coatings. With these data it is difficult to suggest a shape or size effect and it is more likely change sin activity are related to changes in surface area of the silver and hence increased release of silver ions into solution.

Table 1. The silver nanopattern type and antimicrobial activity against *Staphylococcus aureus* and *Pseudomonas aeruginosa* from diffusion-type assay method of using different PS-*b*-PEO systems for different layer of coatings. Statistical analysis: The influence of inhibition zone area with different number of coatings for S1 with silver nanolines and S2 with silver nanodots obtained against *Staphylococcus aureus* and *Pseudomonas aeruginosa.*

Sample	Number of Coating	Pseudomonas		Staphylococcus	
		Inhibition zone[1]	Contact[2]	Inhibition zone[1]	Contact[2]
Blank		0[a]	+	0[a]	+
S1-line	1	92.46 ± 1.42[b]	-	82.78 ± 0.55[b]	-
S2-dot	1	75.12 ± 15.31[c]	-	64.93 ± 0.42[c]	-
S1-line	2	279.58 ± 7.82[d]	-	214.57 ± 1.08[d]	-
S2-dot	2	215.56 ± 19.05[e]	-	168.21 ± 4.85[e]	-
S1-line	4	364.75 ± 4.84[f]	-	282.71 ± 6.88[f]	-
S2-dot	4	276.43 ± 8.35[d]	-	218.25 ± 6.49[d]	-

[1] Inhibitory zone, measured diameter in mm[2].

[2] Contact area under film discs on agar surface; + : growth in the area, − : no growth.

***** Test was carried out in triplicate.

[a,b,c,d,e,f] Different letters in the same column indicate significant differences ($p < 0.05$).

Table 1 clearly demonstrates that repeated silver coatings for both patterns resulted in increased antimicrobial activity towards the gram-positive and gram-negative bacterium. On further coatings, the inhibition zone area does not change measurably. The increases with number of surface coatings is consistent with increasing surface area. It reaches a maximum because further deposition is due to coverage of silver. Greater antimicrobial activity to gram-negative was realized compared to gram-positive for both line and dot patterns similar to previous studies.[40,45] This difference caused by the physical interruption of silver compounds with the bacterial membranes which interacts with cell components leads to interfere of the biochemical processes of cells.[46]

The statistical analysis showed that the number of coatings and the nature of the nanofeature affected the antimicrobial activity by a similar magnitude for both the gram-positive and gram-negative bacterium (Table 1). The highest inhibition area for both *Staphylococcus aureus* and *Pseudomonas aeruginosa* was recorded for glass slides coated 4x with the Ag compared to the less coated samples. The coating affect is not linear with the number of coatings; an increased antimicrobial activity (~50%) was noticed when the number of coating was increased from 1

to 2 significantly higher than that for further coatings for both the nanofeatures. It can also be suggested from the statistical data that similar antimicrobial activity was obtained for nanolines with double coating and nanodots coated 4 times for both the bacteria. Overall, nanolines with 4 times coating had significantly higher antimicrobial activity towards both *Staphylococcus aureus* and *Pseudomonas aeruginosa* compared to nanodots suggesting that surface area is an important antimicrobial factor.

Hwang *et al.* [47] suggested that the dissolution of Ag nanoparticles produced Ag ions and these ions were the reason for toxicity to the bacteria as they react with oxygen to yield reactive oxygen species (ROS). The bacterial activity is also thought to be due to Ag^+ ions which forms "pits" on the membrane surfaces that directly binds thiol groups in the protein cysteine. The enhanced activity to gram-negative bacteria is probably because these have a negatively charged outer layer of lipopolysaccharides followed by a 8 nm thick layer of peptidoglycan. Silver ions easily penetrate these relatively thin layers resulting in protein denaturation and cell death. For the gram-positive bacteria, the much thicker three dimensional rigid peptidoglycan layer (~20–80 nm thick) formed by cross-linking of short peptides and linear polysaccharides limits the ability of Ag^+ to anchor and penetrate the cells.[48] A killing efficiency of silver and composites was also reported supporting this hypothesis.[49] A detailed study has been described earlier.[40,50] Morones *et al*.[46] and Pal *et al.*[51] reported that the silver nanoparticles contained (1 1 1) lattice plane facets were highly reactive and that the abundance of (1 1 1) lattice plane facets had the strongest antimicrobial activity. The XRD analysis (Figure 4e) showed the abundance of (111) lattice plane facets presence which correlates with the antimicrobial activity of the nanopatterns. This does not appear to be a structural effect from the data presented here but is more likely due to the ability of this plane to release ions into solution.

4. CONCLUSIONS

In summary, periodic silver nanolines and dots patterns were generated by an *insitu* inclusion technique into the microphase separated BCP template. By control of polymer molecular weight and the solvent anneal process; the orientation of the self-assembled features can be strictly defined. An ethanol ultrasonication process was optimized to achieve activated templates respectively to allow highly selective incorporation of silver nitrate into the BCP. Spin coating the appropriate concentrations of metal precursor into the template followed by UV/Ozone treatment generates corresponding silver patterns. The average diameters of the nanolines and nanodots were 14 nm and 35 nm respectively. The nanopatterns were polycrystalline. A characteristics plasmon resonance absorption peak was observed in the visible range at around 410 nm and blue-green PL emission was noticed at around 470 nm attributed to Ag^{+} and Ag^{+}- Ag^{+}. The antibacterial activity of both the silver nanopatterns were examined in vitro with *Staphylococcus aureus* (gram-positive bacteria) and *Pseudomonas aeruginosa* (gram-negative bacteria) which reveals greater antimicrobial activity against gram-negative bacteria for both the nanostructures. Importantly, in this work we noticed no significant difference in antibacterial activity as a function of nanofeature size seen on the different nanopattern morphologies. Instead the inhibition zone differences between lines and dots observed varied in a similar way to the nanofeature surface area. This suggests that activity is related to the area of exposed silver. This can be related to the rate of release of Ag^{+} ions into the solution. There is no evidence in this work of antimicrobial activity being related to size induced property changes within silver nanodimensioned objects.

Supporting Information

The supporting information is available free of charge on the ACS publication website.

AFM images with solvent annealing time and different solvents, Height profile for the AFM images.

Notes

The authors declare no competing financial interest.

AUTHOR INFORMATION

Corresponding authors

*E-mail: morrism2@tcd.ie

*E-mail: g_tandra@yahoo.co.in

ACKNOWLEDGEMENTS

We acknowledge financial support from the Science Foundation Ireland AMBER grant 12/RC/2278. We would also like to thank Dr. Michael Schmidt for the TEM assistance.

REFERENCES

(1) Yan, C. Y.; Kang, W. B.; Wang, J. X.; Cui, M. Q.; Wang, X.; Foo, C. Y.; Chee, K. J.; Lee, P. S. Stretchable and Wearable Electrochromic Devices. *ACS Nano* **2014**, *8*, 316-322.

(2) Joo, Y.; Byun, J.; Seong, N.; Ha, J.; Kim, H.; Kim, S.; Kim, T.; Im, H.; Kim, D.; Hong, Y. Silver Nanowire-embedded PDMS With a Multiscale Structure for a Highly Sensitive and Robust Flexible Pressure Sensor. *Nanoscale* **2015**, *7*, 6208-6215.

(3) Kabashin, A. V.; Evans, P.; Pastkovsky, S.; Hendren, W.; Wurtz, G. A.; Atkinson, R.; Pollard, R.; Podolskiy, V. A.; Zayats, A. V. Plasmonic Nanorod Metamaterials for Biosensing. *Nat. Mater.* **2009**, *8*, 867-871.

(4) Santos, A.; Deen, M. J.; Marsal, L. F. Low-cost Fabrication Technologies for Nanostructures: State-of-the-art and Potential. *Nanotechnology* **2015**, *26*, 20.

(5) Lee, M. S.; Lee, K.; Kim, S. Y.; Lee, H.; Park, J.; Choi, K. H.; Kim, H. K.; Kim, D. G.; Lee, D. Y.; Nam, S.; Park, J. U. High-Performance, Transparent, and Stretchable Electrodes using Graphene-Metal Nanowire Hybrid Structures. *Nano Lett.* **2013**, *13*, 2814-2821.

(6) Kim, S.; Kim, S. Y.; Kim, J.; Kim, J. H. Highly Reliable AgNW/PEDOT:PSS Hybrid Films: Efficient Methods for Enhancing Transparency and Lowering Resistance and Haziness. *J. Mater. Chem. C* **2014**, *2*, 5636-5643.

(7) Emerging Research Devices. In *The International Technology Roadmap for Semiconductors*, 2011; pp 1-77.

(8) Borah, D.; Ozmen, M.; Rasappa, S.; Shaw, M. T.; Holmes, J. D.; Morris, M. A. Molecularly Functionalized Silicon Substrates for Orientation Control of the Microphase Separation of PS-b-PMMA and PS-b-PDMS Block Copolymer Systems. *Langmuir* **2013**, *29*, 2809-2820.

(9) Wang, Q.; Nealey, P. F.; de Pablo, J. J. Monte Carlo Simulations of Asymmetric Diblock Copolymer Thin Films Confined between Two Homogeneous Surfaces. *Macromolecules* **2001**, *34*, 3458-3470.

(10) Rasappa, S.; Borah, D.; Faulkner, C. C.; Lutz, T.; Shaw, M. T.; Holmes, J. D.; Morris, M. A. Fabrication of a Sub-10 nm Silicon Nanowire Based Ethanol Sensor using Block Copolymer Lithography. *Nanotechnology* **2013**, *24,* 065503-1-8.

(11) Borah, D.; Shaw, M. T.; Rasappa, S.; Farrell, R. A.; O'Mahony, C.; Faulkner, C. M.; Bosea, M.; Gleeson, P.; Holmes, J. D.; Morris, M. A. Plasma Etch Technologies for the Development of Ultra-small Feature Size Transistor Devices. *J. Phys. D-Appl. Phys.* **2011**, *44*, 174012-1-12.

(12) Zhao, J. C.; Jiang, S. C.; Ji, X. L.; An, L. J.; Jiang, B. Z. Study of the Time Evolution of the Surface Morphology of Thin Asymmetric Diblock Copolymer Films Under Solvent Vapor. *Polymer* **2005**, *46*, 6513-6521.

(13) Mokarian-Tabari, P.; Collins, T. W.; Holmes, J. D.; Morris, M. A. Cyclical "Flipping" of Morphology in Block Copolymer Thin Films. *ACS Nano* **2011**, *5*, 4617-4623.

(14) Segalman, R. A.; Yokoyama, H.; Kramer, E. J. Graphoepitaxy of Spherical Domain Block Copolymer Films. *Adv. Mater.* **2001**, *13*, 1152-1155.

(15) Thurn-Albrecht, T.; Schotter, J.; Kastle, C. A.; Emley, N.; Shibauchi, T.; Krusin-Elbaum, L.; Guarini, K.; Black, C. T.; Tuominen, M. T.; Russell, T. P. Ultrahigh-density Nanowire Arrays Grown in Self-assembled Diblock Copolymer Templates. *Science* **2000**, *290*, 2126-2129.

(16) Cheng, J. Y.; Mayes, A. M.; Ross, C. A. Nanostructure Engineering by Templated Self-assembly of Block Copolymers. *Nat. Mater.* **2004**, *3*, 823-828.

(17) De Rosa, C.; Park, C.; Thomas, E. L.; Lotz, B. Microdomain Patterns from Directional Eutectic Solidification and Epitaxy. *Nature* **2000**, *405*, 433-437.

(18) Fasolka, M. J.; Mayes, A. M. Block Copolymer Thin Films: Physics and Applications. *Ann. Rev. Mater. Res.* **2001**, *31*, 323-355.

(19) Ghoshal, T.; Shaw, M. T.; Bolger, C. T.; Holmes, J. D.; Morris, M. A. A General Method for Controlled Nanopatterning of Oxide Dots: A Microphase Separated Block Copolymer Platform. *J. Mater. Chem.* **2012**, *22*, 12083-12089.

(20) Ghoshal, T.; Maity, T.; Godsell, J. F.; Roy, S.; Morris, M. A. Large Scale Monodisperse Hexagonal Arrays of Superparamagnetic Iron Oxides Nanodots: A Facile Block Copolymer Inclusion Method. *Adv. Mater.* **2012**, *24*, 2390-2397.

(21) Ghoshal, T.; Senthamaraikannan, R.; Shaw, M. T.; Holmes, J. D.; Morris, M. A. Fabrication of Ordered, Large Scale, Horizontally-Aligned Si Nanowire Arrays Based on an In Situ Hard Mask Block Copolymer Approach. *Adv. Mater.* **2014,** *26*, 1207-1216.

(22) Ghoshal, T; Maity, T; Senthamaraikannan, R; Shaw, M; Carolan, P; Holmes, J; Roy, S; Morris, M. A. Size and Space Controlled Hexagonal Arrays of Superparamagnetic Iron Oxide Nanodots: Magnetic Studies and Application. *Scientific Reports* **2013,** *3*, 2772-1-8.

(23) Ghoshal, T; Fleming, P. G; Holmes, J. D; Morris, M. A. The Stability of ‘‘Ce_2O_3’’ Nanodots in Ambient Conditions: A Study Using Block Copolymer Templated Structures. *J. Mater. Chem.* **2012,** 22, 22949-22957.

(24) Zhang, M. F; Yang, L; Yurt, S; Misner, M. J; Chen, J. T; Coughlin, E. B; Venkataraman, D; Russell, T. P. Highly Ordered Nanoporous Thin Films from Cleavable Polystyrene-*block*-poly(ethylene oxide). *Adv. Mater.,* **2007**, 19, 1571-1576.

(25) Mao, H. M; Hillmyer, M. A. Nanoporous Polystyrene by Chemical Etching of Poly(ethylene oxide) from Ordered Block Copolymers. *Macromolecules,* **2005**, 38, 4038-4039.

(26) Huang, E; Mansky, P; Russell, T. P; Harrison, C; Chaikin, P. M; Register, R. A. Hawker, C. J; Mays, J. Mixed Lamellar Films: Evolution, Commensurability Effects and Preferential Defect Formation. *Macromolecules,* **2000,** 33, 80-88.

(27) Tseng, Y. C; Peng, Q; Ocola, L. E; Elam, J. W; Darling, S. B. Enhanced Block Copolymer Lithography Using Sequential Infiltration Synthesis. *J. Phys. Chem. C,* **2011**, 115, 17725-17729.

(28) Akter, T.; Kim, W. S. Reversibly Stretchable Transparent Conductive Coatings of Spray-Deposited Silver Nanowires. *ACS Appl. Mater. Interfaces* **2012**, *4*, 1855-1859.

(29) Lee, H.; Lee, K.; Park, J. T.; Kim, W. C.; Lee, H. Well-Ordered and High Density Coordination-Type Bonding to Strengthen Contact of Silver Nanowires on Highly Stretchable Polydimethylsiloxane. *Adv. Funct. Mater.* **2014**, *24*, 3276-3283.

(30) Chang, J. H.; Chiang, K. M.; Kang, H. W.; Chi, W. J.; Chang, J. H.; Wu, C. I.; Lin, H. W. A Solution-processed Molybdenum Oxide Treated Silver Nanowire Network: A Highly Conductive Transparent Conducting Electrode with Superior Mechanical and Hole Injection Properties. *Nanoscale* **2015**, *7*, 4572-4579.

(31) Hu, L. B.; Kim, H. S.; Lee, J. Y.; Peumans, P.; Cui, Y. Scalable Coating and Properties of Transparent, Flexible, Silver Nanowire Electrodes. *ACS Nano* **2010**, *4*, 2955-2963.

(32) Donlan, R. M. Biofilms and Device-associated Infections. *Emerg. Infect. Dis* **2001**, *7*, 277-281.

(33) Cagri, A.; Ustunol, Z.; Ryser, E. T. Antimicrobial Edible Films and Coatings. *J. Food Prot.* **2004**, *67*, 833-848.

(34) Rizzello, L.; Pompa, P. P. Nanosilver-based Antibacterial Drugs and Devices: Mechanisms, Methodological Drawbacks, and Guidelines. *Chem. Soc. Rev.* **2014**, *43*, 1501-1518.

(35) Mijnendonckx, K.; Leys, N.; Mahillon, J.; Silver, S.; Van Houdt, R. Antimicrobial Silver: Uses, Toxicity and Potential for Resistance. *Biometals* **2013**, *26*, 609-621.

(36) Gu, X. D.; Liu, Z. W.; Gunkel, I.; Chourou, S. T.; Hong, S. W.; Olynick, D. L.; Russell, T. P. High Aspect Ratio Sub-15 nm Silicon Trenches From Block Copolymer Templates. *Adv. Mater.* **2012**, *24*, 5688-5694.

(37) Zhao, Y. Y; Bao, C. G; Feng, R; Mason, T. J. New Etching Method of PVC Plastic for Plating by Ultrasound. *J. Appl. Polym. Sci.* **1998**, 68, 1411-1416.

(38) Ho, D. L; Hammouda, B; Kline, S. R; Chen, W. R. Unusual Phase Behavior in Mixtures of Poly(ethylene oxide) and Ethyl alcohol. *J. Polym. Sci. Pt. B-Polym. Phys.* **2006,** 44, 557-564.

(39) Thorat, A. V.; Ghoshal, T.; Morris, M. A. Silver Nanopatterned Surfaces by Block Copolymer Inclusion and Biomineralization. *Advanced Science, Engineering and Medicine* **2016**, *8*, 1-8.

(40) Azlin-Hasim, S.; Cruz-Romero, M. C.; Ghoshal, T.; Morris, M. A.; Cummins, E.; Kerry, J. P. Application of Silver Nanodots for Potential use in Antimicrobial Packaging Applications. *Innov. Food Sci. Emerg. Technol.* **2015**, *27*, 136-143.

(41) Kumar, D.; Kavita; Singh, K.; Verma, V.; Bhatti, H. S. Microwave-assisted Synthesis and Characterization of Silver Nanowires by Polyol Process. *Appl. Nanosci.* **2015**, *5*, 881-890.

(42) Das, R.; Nath, S. S.; Chakdar, D.; Gope, G.; Bhattacharjee, R. Synthesis of Silver Nanoparticles and Their Optical Properties. *J. Exp. Nanosci.* **2010**, *5*, 357-362.

(43) Sarkar, R.; Kumbhakar, P.; Mitra, A. K.; Ganeev, R. A. Synthesis and Photoluminescence Properties of Silver Nanowires. *Curr. Appl. Phys.* **2010**, *10*, 853-857.

(44) Parang, Z.; Keshavarz, A.; Farahi, S.; Elahi, S. M.; Ghoranneviss, M.; Parhoodeh, S. Fluorescence Emission Spectra of Silver and Silver/cobalt Nanoparticles. *Sci. Iran.* **2012**, *19*, 943-947.

(45) Shrivastava, S.; Bera, T.; Roy, A.; Singh, G.; Ramachandrarao, P.; Dash, D. Characterization of Enhanced Antibacterial Effects of Novel Silver Nanoparticles. *Nanotechnology* **2007**, *18*, 225103-1-9.

(46) Morones, J. R.; Elechiguerra, J. L.; Camacho, A.; Holt, K.; Kouri, J. B.; Ramirez, J. T.; Yacaman, M. J. The Bactericidal Effect of Silver Nanoparticles. *Nanotechnology* **2005**, *16*, 2346-2353.

(47) Hwang, E.T; Lee, J. H; Chae, Y.J.; Kim, Y.S; Kim, B. C; Sang, B.-I; Gu, M. B. Analysis of the Toxic Mode of Action of Silver Nanoparticles using Stress-specific Bioluminescent Bacteria. *Small* **2008**, 4,746-750.

(48) Holt, K. B.; Bard, A. J. Interaction of Silver(I) Ions with the Respiratory Chain of Escherichia Coli: An Electrochemical and Scanning Electrochemical Microscopy Study of the Antimicrobial Mechanism of Micromolar Ag. *Biochemistry* **2005**, *44*, 13214-13223.

(49) Li, X; Gao, P; Tan, J; Xiong, K; Maitz, M. F; Pan, C;Wu, H; Chen, Y;Yang, Z; Huang, N. Assembly of Metal−Phenolic/Catecholamine Networks for Synergistically Anti-Inflammatory, Antimicrobial, and Anticoagulant Coatings. *ACS appl. Mater. Interfaces* **2018**, 10, 40844-40853.

(50) Azlin-Hasim, S.; Cruz-Romero, M. C.; Morris, M. A.; Cummins, E.; Kerry, J. P. Effects of a Combination of Antimicrobial Silver Low Density Polyethylene Nanocomposite Films and Modified Atmosphere Packaging on the Shelf Life of Chicken Breast Fillets. *Food pack. Shelf life.* **2015**, *4*, 26-35.

(51) Pal, S; Tak, Y. K; Song, J. M. Does the Antibacterial Activity of Silver Nanoparticles Depend on the Shape of the Nanoparticle? A Study of the Gram-negative Bacterium Escherichia Coli. *Applied and environmental Microbiology* **2007**, 73, 1712–1720.

Scheme 1. Schematic illustration of the fabrication of silver (I) nanodots and (II) nanoline patterns on substrate. (A) PEO cylinders (I) perpendicular and (II) parallel to the substrate in the PS matrix after solvent annealing (B) Modification of PEO cylinders creates nanoporous template (C) silver precursor solution spin coated on the template (D) silver (I) nanodots and (II) nanoline patterns formed after UV/ozone treatment.

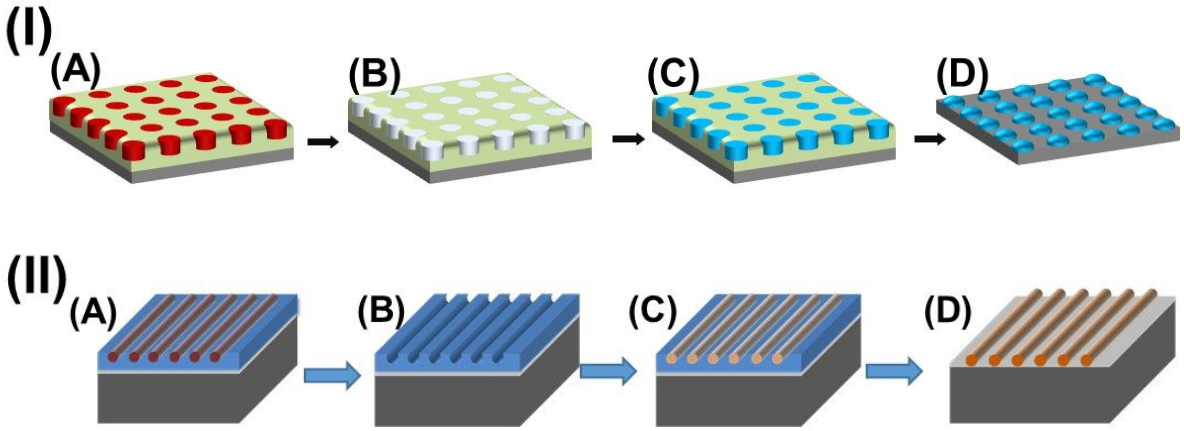

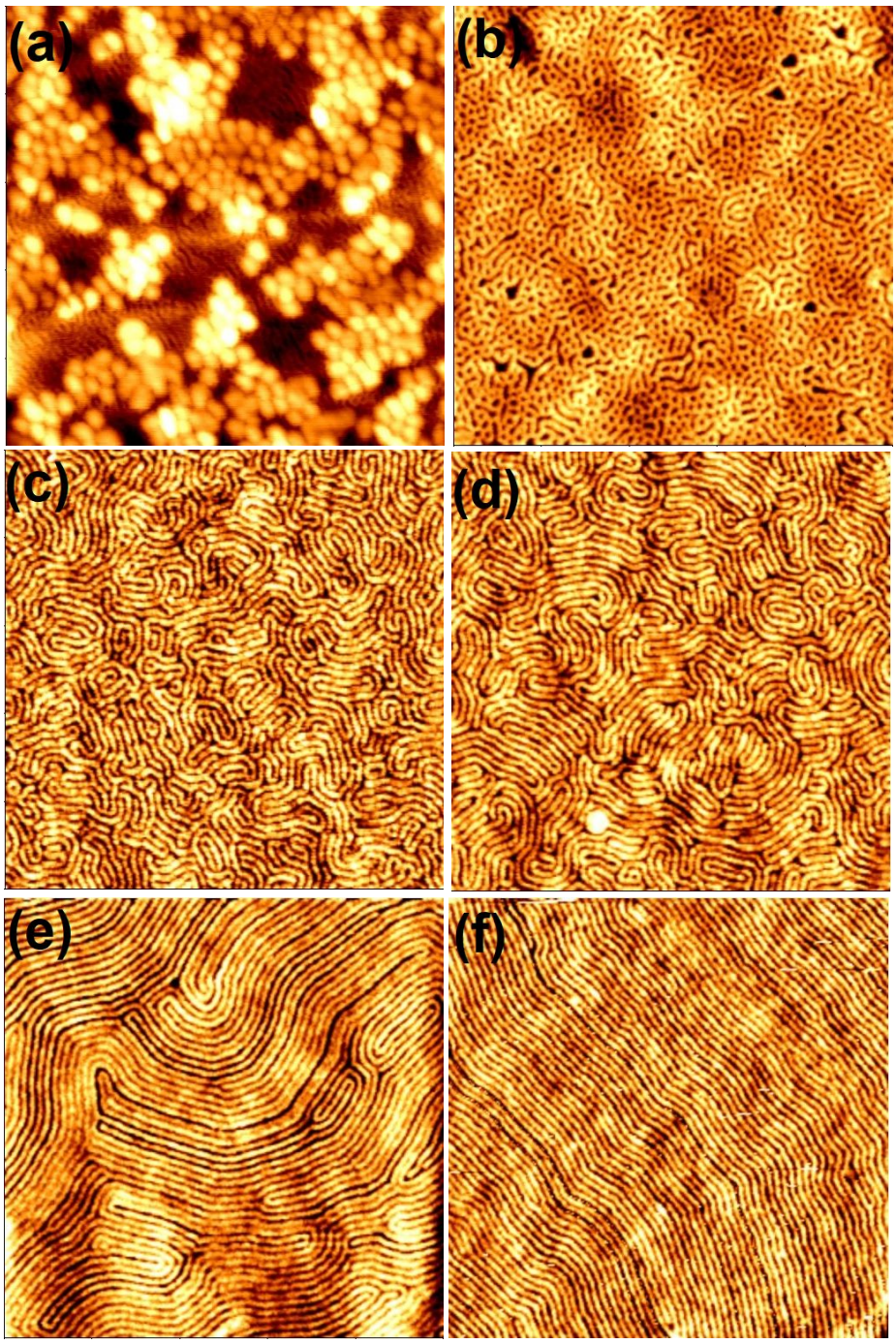

Figure 1. Tapping mode AFM images for BCP S1 PS-PEO (32k-11k) after the toluene exposure at 50° C for different time period of (a) 15 min, (b) 30 min, (c) 1 h, (d) 1 h 30 min, (e) 2 h and (f) 3 h. All images scale bar 2 x 2 μm^2.

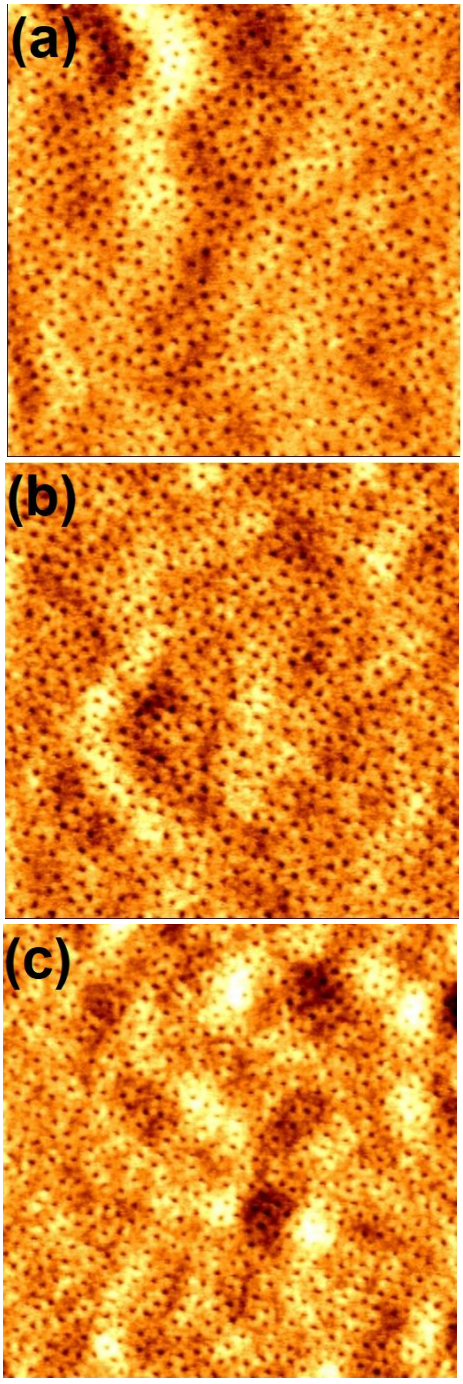

Figure 2. Tapping mode AFM images for BCP S2 PS-PEO (62k-16k) under toluene/THF exposure at 60° C for different time period of (a) 30 min, (b) 1 h and (c) 1 h 30 min. All images scale bar 2 x 2 μm^2.

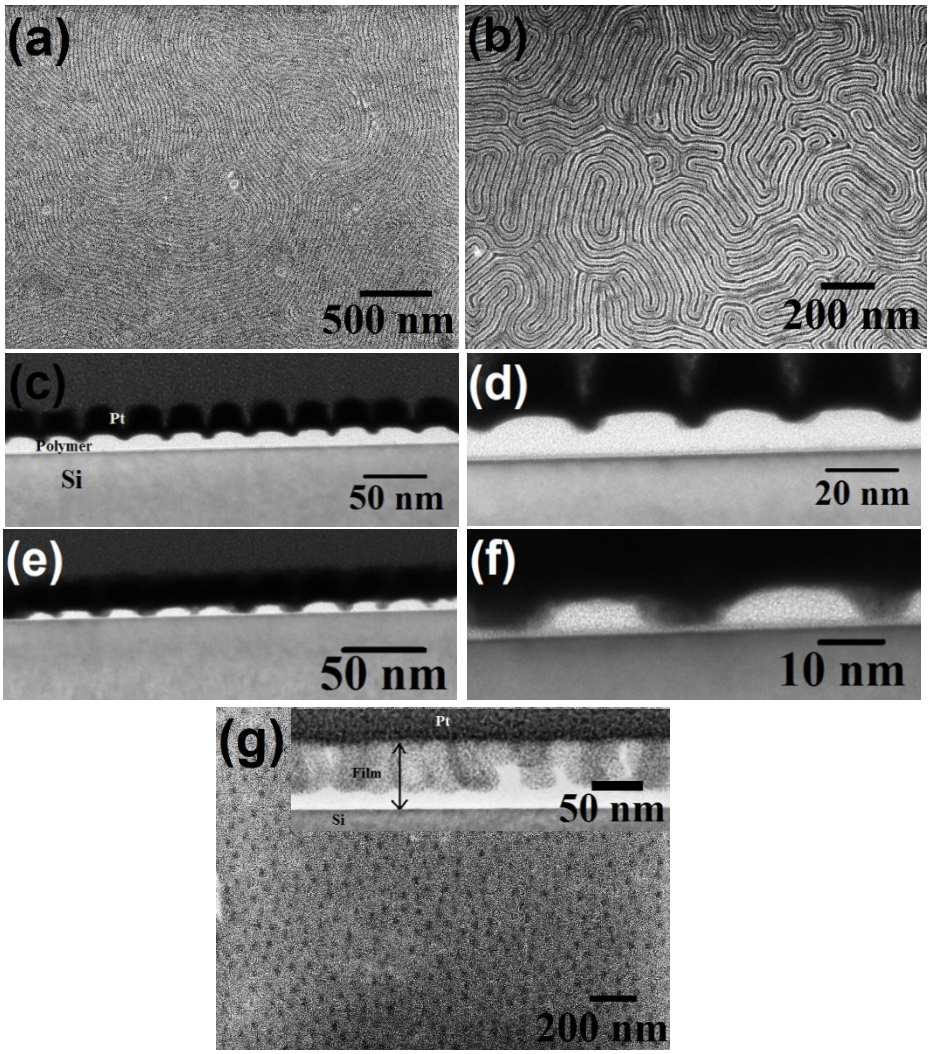

Figure 3. SEM images of the nanoporous (a, b) line and (g) dot templates after ethanol exposure of S1 and S2 respectively. FIB cross-sectioned TEM images of the nanoporous line template after ethanol ultrasonication for (c, d) 14 min and (e, f) 18 minutes respectively. Inset of (g) shows cross-sectioned TEM image of S2 after ethanol ultrasonication for 22 minutes.

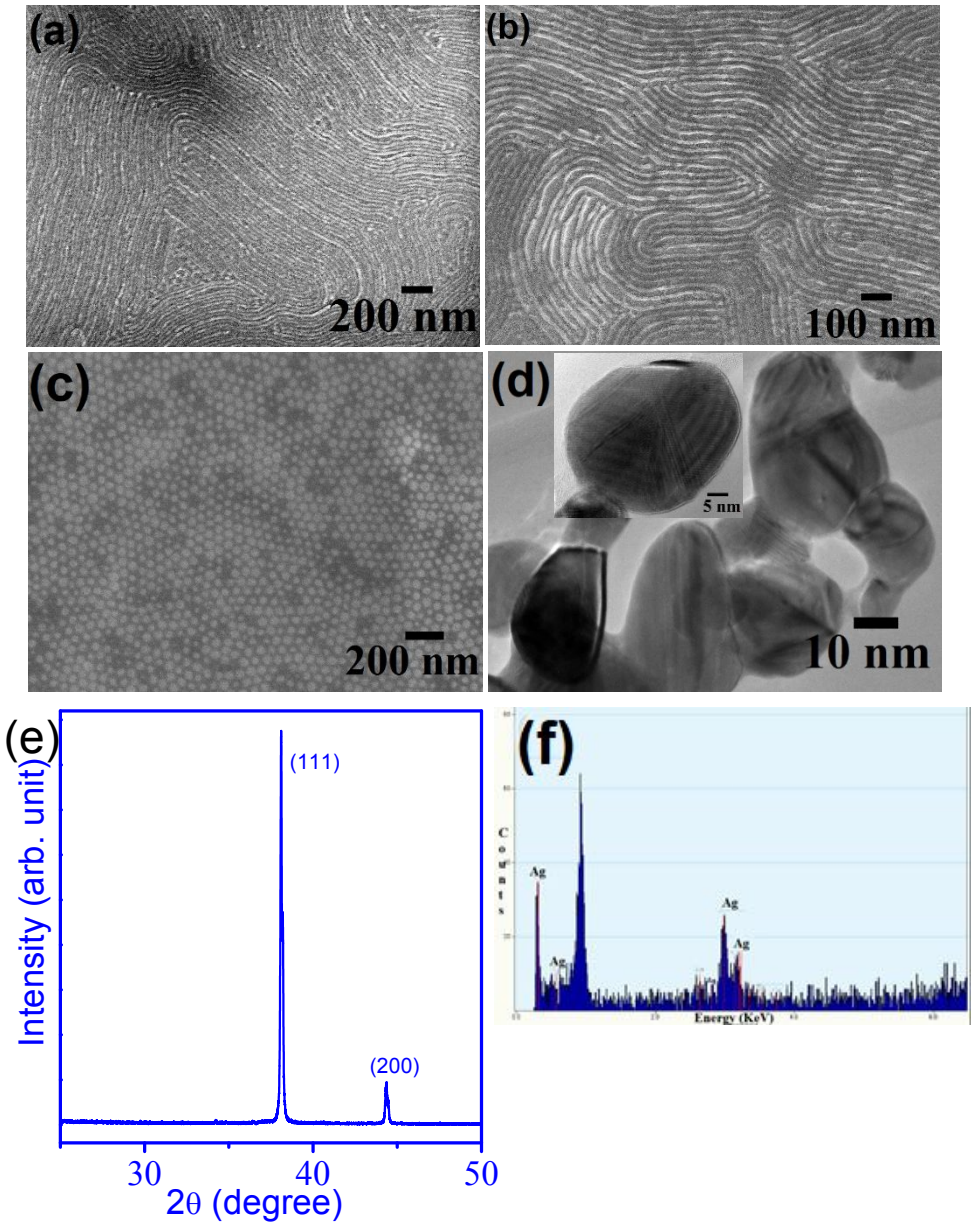

Figure 4. SEM images of silver (a, b) nanoline and (c) nanodot arrays. (d) TEM and inset of (d) HRTEM image of silver nanodots. Representative (e) XRD and (f) EDX spectrum of silver nanostructure arrays.

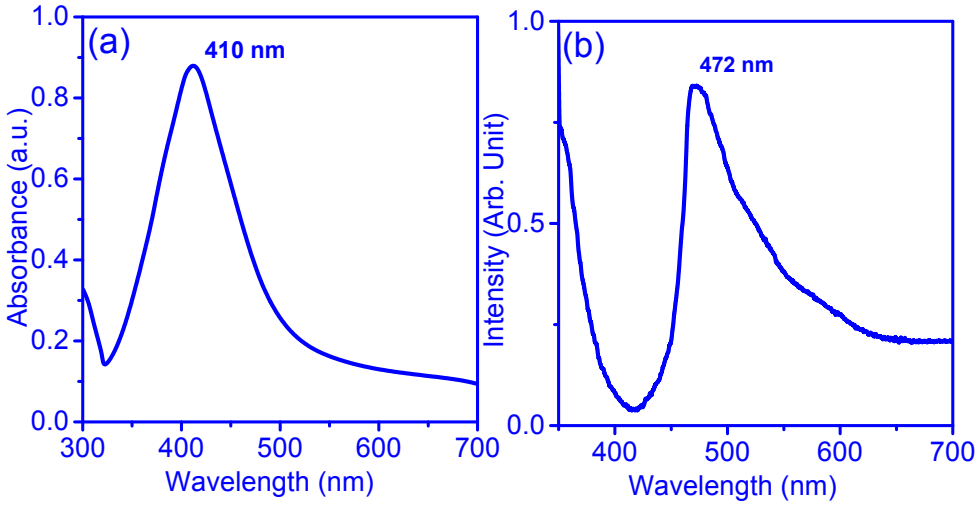

Figure 5. (a) Uv-vis and (b) photoluminescence spectra of silver nanostructure arrays.

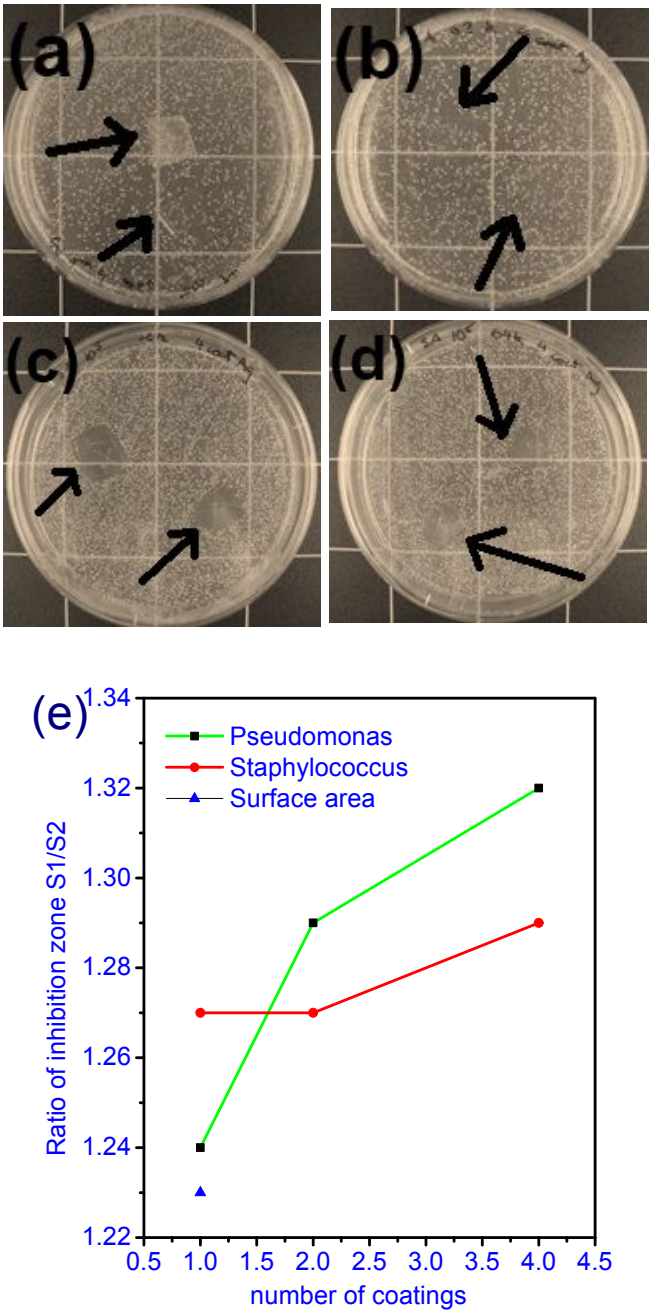

Figure 6. Antibacterial activity of silver nanopatterns in vitro with two different kind of bacteria Staphylococcus (gram positive bacteria) (a, nanolines; b, nanodots) and Pseudomonas (gram negative bacteria) (c, nanolines; d, nanodots) respectively. (e) The ratio of inhibition zone area and the surface area of silver nanopatterns between S1 and S2 with the increased number of coatings.

Table of contents:

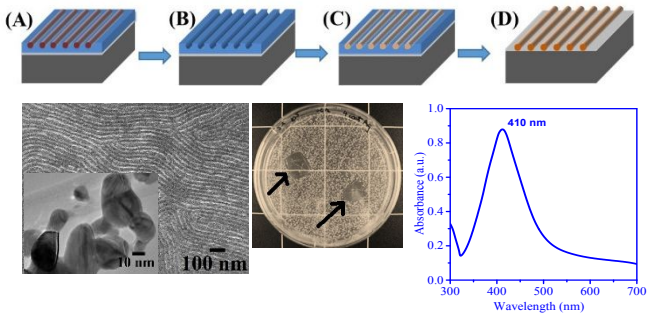

Table of contents: